

Carbon Supports Mitigate Resistivity Limitations in Ni–Mo Alkaline Hydrogen Evolution Electrocatalysts

Rituja B. Patil,[†] Aayush Mantri,^{†,‡} Stephen D. House,[†] Judith C. Yang,[†] and
James R. McKone^{*,†}

[†]*Department of Chemical and Petroleum Engineering, University of Pittsburgh, Pittsburgh,
PA, 15260, USA*

[‡]*Current affiliation: H-Quest Vanguard Inc., Pittsburgh, PA, USA*

E-mail: jmckone@pitt.edu

Phone: +1 (412)-384-7407

Abstract

Alkaline water electrolysis offers the use of low-cost active materials and ancillary components, making it attractive for renewable hydrogen production. Nevertheless, the practical performance of non-precious electrocatalysts for alkaline hydrogen evolution still lags behind platinum-group metals. This disparity motivates continued work to understand how the solid-state chemistry of non-precious transition metal alloys influences their activity toward alkaline hydrogen evolution. To this end, we have clarified the composition, chemical structure, and morphology of a previously reported Ni–Mo nanopowder electrocatalyst. The as-synthesized catalyst is mixed phase—comprising crystalline Ni-rich alloy nanoparticles embedded in a Mo-rich oxide matrix—and exhibits low activity toward hydrogen evolution. Its alkaline hydrogen evolution activity

greatly increases upon activation by post-deposition reductive annealing or by including carbon black as a catalyst support. These results are consistent with a physical picture in which activity is limited not by kinetics, but by electrical resistivity arising from thin oxide layers at the interfaces between Ni–Mo nanoparticles. Additional efforts to optimize the dispersion of Ni–Mo nanopowders on carbon black supports resulted in mass activities exceeding 60 mA/mg (on the basis of Ni–Mo mass) at 100 mV overpotential. This is over 5-fold greater than we observed for activation by hydrogen annealing, and we postulate that these Ni–Mo/C films are still limited in part by electrical resistivity.

Keywords

electrochemistry; electrocatalysis; alkaline electrolysis; hydrogen evolution; nickel; Ni; molybdenum; Mo; Ni–Mo nanopowder; carbon black; alloy; oxide; conductivity; resistivity

Introduction

Hydrogen is a vital commodity chemical, important as a feedstock to sustain heavy-volume industries like ammonia synthesis, methanol production, and petroleum refining.¹ Hydrogen is also useful as a fuel, and it is widely considered as a sustainable alternative to fossil resources for transportation and energy storage.² Currently, hydrogen production is dominated by fossil-fuel based methods like steam reforming and coal gasification. These schemes are problematic since they operate on non-renewable feedstocks and result in harmful carbon emissions. By contrast, water electrolysis from renewable electricity offers an attractive platform for large-scale hydrogen production in the future.

While electrolyzer systems are technologically mature, their large-scale implementation is still limited by high capital and operating costs.³ Two types of water electrolyzer that have seen extensive laboratory and commercial development are based on aqueous alkali

and proton-exchange membrane (PEM) electrolytes. Liquid alkaline electrolyzers are characterized by their use of non-precious catalysts for the hydrogen evolution reaction (HER) at the cathode and the oxygen evolution reaction (OER) at the anode. However, alkaline electrolyzers operate at relatively low current densities and energy efficiencies, which makes them suitable mainly in locations where large quantities of low cost electricity are available, such as hydroelectric facilities.⁴ PEM electrolyzers operate with characteristically higher energy efficiencies even at very high current densities due in part to the use of very thin layers of precious metal catalysts for the HER and OER.⁵ Nevertheless, large-scale hydrogen production by PEM electrolyzers remains challenging due to the high costs for these active layers and for ancillary components that must be corrosion resistant to operate in acid environments.⁶

Recent interest has grown in alkaline anion exchange membrane (AAEM) electrolyzers as a way to combine the benefits of PEM and liquid alkaline systems.^{7–11} AAEMs are structurally and operationally comparable to PEMs, but they conduct hydroxide ions instead of protons. This enables AAEM electrolyzers to use catalyst materials and balance-of-plant components that are considerably lower in cost than in PEM electrolyzers, while also potentially achieving high efficiencies and reaction rates. Thus, active research is oriented toward synthesis and benchmarking AAEMs that display suitable stability and hydroxide ion conductivity.^{11–16} Analogous work is also focused on the discovery, characterization, and benchmarking of alkaline hydrogen^{17–26} and oxygen evolution electrocatalysts.^{27–37} In this context, we are studying Ni–Mo composites for alkaline hydrogen evolution, with the ultimate goal of closing the gap in activity between non-precious and Pt-based HER catalysts.

Pure Ni cathodes exhibit moderate activity toward alkaline hydrogen evolution, which can be enhanced by alloying with one or more additional transition metals.^{13,19} Alloys and intermetallic compounds containing Ni and Mo have shown particular promise.^{28,38} For example, Brown et al. synthesized Ni–Mo alloy on Ni and steel current collectors by a pyrolysis-reduction method.³⁹ These cathodes exhibited remarkable HER activities exceeding 1 A/cm²

current density at <100 mV overpotential, and were stable for over a year in 30 wt% KOH at 70 °C. Raj et al. reported extensively on electrodeposition of Ni-based alloys and consistently found that binary and ternary cathodes containing Ni and Mo gave the best performance.^{40–42} Gao et al. reported high surface-area Ni–Mo microspheres electrodeposited on Cu that exhibited HER activity of 20 mA/cm² at 63 mV overpotential in 1 M KOH at room temperature.⁴³ Electrodeposition of Ni₄Mo on Cu-foam also lead to remarkably low overpotentials of 34 mV at 20 mA/cm² in 1 M NaOH at room temperature.⁴⁴ Another Ni₄Mo catalyst was synthesized by hydrothermal precipitation and thermal reduction, which yielded 10 mA/cm² at 15 mV overpotential in 1 M KOH at room temperature.⁴⁵ McCrory et al. electrodeposited a wide range of hydrogen evolution electrocatalysts and found that Ni–Mo alloys exhibited alkaline HER activity and stability that was competitive with smooth Pt electrodes.²⁰ These reports, along with numerous others,^{46–69} illustrate the attractiveness of alkaline HER catalysts based on mixtures of Ni and Mo. Nevertheless, these prior studies encompass a wide range of catalyst compositions, morphologies, and mass loadings. Thus, the reported geometric current densities and overpotential performance also varied widely, in spite of the fact that active sites may be similar between various types of Ni–Mo. This motivates continued work to understand the precise composition and activity of Ni–Mo alkaline HER electrocatalysts.

The focus of this study was on Ni–Mo alloy nanopowders synthesized by serial precipitation of mixed Ni–Mo oxides followed by thermal reduction under hydrogen gas. Previous work on these Ni–Mo nanopowders resulted in HER activities exceeding 10 mA/cm² at 100 mV overpotential at room temperature in alkaline aqueous electrolyte at mass loadings on the order of 1 mg/cm².⁷⁰ Ni–Mo nanopowder has also been used in hydrogen-evolving photocathodes and full solar water splitting devices.^{71,72} Ni–Mo alloys obtained by similar methods have achieved 700 mA/cm² at 150 mV overpotential in 5 M KOH at 70 °C when deposited at high mass loadings (tens of mg/cm²) on Ni foam substrates.⁷³ Several reports have also emerged in which Ni–Mo nanopowders were used as cathodes in functional AAEM

and alkaline water electrolysis assemblies.^{10,46}

Building on these prior studies, we report here new insights into the composition and structure of Ni–Mo nanopowder electrocatalysts. We found that Ni–Mo synthesized by two different precipitation-reduction methods—one using ammonia-based precursors and another based on a simple salt metathesis reaction without ammonia—were multi-phase, consisting of a Ni-rich face-centered cubic (fcc) alloy component coated with a nearly conformal layer of Mo-rich oxide. Importantly, the as-synthesized nanopowder exhibited only modest HER activity in alkaline aqueous electrolytes; an additional thermal annealing step following deposition on a substrate was required to activate the catalyst.⁷⁰ We were able to achieve a similar activating effect by instead incorporating carbon black into the oxide precursor prior to reduction to the final Ni–Mo catalyst. Based on these results, we conclude that the observed activity is limited primarily by inter-particle electrical resistivity rather than kinetics or mass transfer. We have formulated a mathematical model that reproduces these effects by simulating a combination of reaction kinetics and electrical resistivity in a 1-dimensional chain of nanoparticles separated by thin oxide layers. Additional efforts to optimize Ni–Mo/C dispersion resulted in HER activities (based on the mass of the Ni–Mo) that were 6-fold greater than carbon-free nanopowders that were synthesized under otherwise identical conditions and activated by thermal annealing.

Experimental

A detailed discussion of experimental methods, including materials and reagents, synthetic methods, and analytical procedures are provided in the Supporting Information. Briefly, we synthesized Ni–Mo nanopowder composites via serial precipitation and thermal reduction reactions, analogous to several prior reported syntheses.^{39,45,70} Two different approaches were used to precipitate mixed Ni–Mo oxides from aqueous solution. The first was an ammonia-based reaction that began with a 6:4 mole ratio of Ni and Mo. This synthesis was essentially

identical to a previously reported procedure.⁷⁰ However, the ratio of Ni and Mo changed to 7:3 in the oxides and in the reduced powder, indicating Mo loss during the synthesis or during oxide purification. In a second ammonia-free precipitation reaction, equimolar aqueous solutions of sodium molybdate and nickel chloride were mixed and heated in the presence of diethylene glycol to precipitate hydrated NiMoO_4 . This latter procedure was developed to eliminate ammonia from the synthesis in favor of NaCl as a comparatively nonhazardous byproduct. In a typical precipitation, the precursors were first dissolved in water, mixed with a suitable quantity of diethylene glycol, and heated on a ceramic hotplate with stirring for several minutes to precipitate a solid mixed oxide precipitate. The reaction mixture was then centrifuged and washed several times with water and organic solvents to separate out the oxides.

To prepare Ni-Mo/C catalyst composites, a mixture of the precursor oxides and Vulcan carbon black were obtained by physical grinding with a mortar and pestle for 15 minutes, or by carrying out the associated precipitation reaction in the presence of Vulcan carbon. Precursor composites were prepared targeting final carbon contents of 10, 25, 50, 75, and 90 wt% relative to total Ni-Mo/C mass. Ni-Mo oxides were also deposited directly on Ni mesh substrates by a flame pyrolysis method, following a previous report.³⁹ Nanostructured Ni catalysts were synthesized by another precipitation-reduction method, wherein aqueous Ni nitrate was added to concentrated KOH to cause instant precipitation of nickel hydroxide, which was again purified by centrifugation. In all cases, the precursor mixtures were converted to active catalysts by thermal reduction under forming gas in a tube furnace first at 200°C for 30 minutes and then at 450–550 °C for 1 hour.

Reaction products were analyzed with respect to composition and crystallinity using X-ray diffraction (XRD), scanning electron microscopy (SEM), transmission electron microscopy (TEM), and energy-dispersive X-ray spectroscopy (EDS). Thermogravimetric analysis (TGA) was used to measure the mass ratio of carbon to transition metals via sequential oxidation to remove carbon (along with concomitant regeneration of mixed metal oxides)

followed by hydrogen reduction to again remove oxygen. Catalyst films were coated onto suitable substrates from alcoholic colloids, and their catalytic activity toward alkaline hydrogen evolution was characterized using cyclic voltammetry. In some cases Nafion ionomer was included as a binder in the colloidal solutions, and in other cases catalyst films were subjected to post-deposition thermal annealing to improve adhesion and catalytic activity. Simulations were executed using the Matlab software suite to formulate and numerically solve algebraic equations that describe contributions to overpotential from reaction kinetics and inter-particle resistivity.

Results and Discussion

Figure 1 shows XRD results for Ni–Mo oxides and catalysts synthesized by the ammonia-based and ammonia-free methods. The oxides synthesized in the presence of ammonia ex-

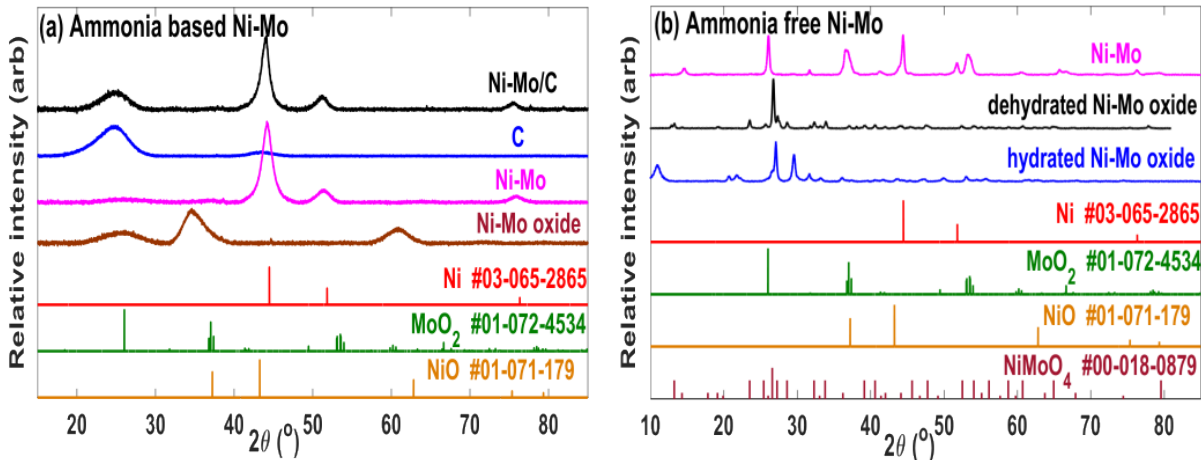


Figure 1: X-ray diffraction patterns of intermediates and products associated with (a) ammonia-based and (b) ammonia-free Ni–Mo nanopowders. Standard diffraction patterns corresponding to the indexed compounds are also included and labeled with card numbers corresponding to entries in the ICDD PDF database.

hibited broad diffraction features at $2\Theta = 25, 35,$ and 61° . The breadth of these peaks indicates that the products were poorly crystalline, and we were unable to index them to any known compound containing Ni, Mo, or composites containing both elements. The

as-synthesized oxides from the ammonia-free synthesis gave diffraction patterns that closely resemble hydrated NiMoO_4 as reported by Brito.⁷⁴ As further evidence of a hydrous product, the ammonia-free precursor oxides could be converted to crystalline NiMoO_4 after a heat treatment in air at 400 °C for 30 minutes.

Upon reduction, Ni–Mo composite nanopowders with and without carbon additives gave diffraction features consistent with face-centered cubic (fcc) Ni. The carbon-containing samples also showed a broad feature at $2\Theta \sim 24^\circ$, matching that of Vulcan carbon black alone. Peak positions were shifted slightly to lower 2Θ values than in pure Ni, which is attributable to lattice expansion arising from the incorporation of Mo into the Ni lattice, as has been reported previously.⁶⁰ By application of Bragg’s law to the fcc peaks, we extracted a lattice constant of 3.56 Å for the ammonia-based synthesis and 3.57 Å for the ammonia-free synthesis, implying Mo content of 9.25 mol% and 10.6 mol% in the alloy respectively. We estimate an error of ± 1 mol% in the Mo content values. Thus, the Mo content of these alloys was mutually similar and considerably lower than the Mo mole fraction incorporated into the synthesis in both cases. The ammonia-free product also gave diffraction features consistent with crystalline MoO_2 , which accounts for the additional Mo in excess of that incorporated into the alloy. Careful inspection of the ammonia-based Ni–Mo XRD pattern baseline also showed evidence of poorly crystalline MoO_2 and NiO (see Supporting Information). Based on these results, we broadly conclude that the ammonia-based and the ammonia-free syntheses gave rise to compositionally similar mixed phase Ni–Mo products.

Figure 2 depicts micrographs of Ni–Mo oxides and unsupported Ni–Mo nanopowder composites by both synthesis routes. Ammonia-based nanopowders were irregular agglomerates of nanoparticles that were several hundred nm in diameter both in the oxide and the reduced product. By contrast, the ammonia-free synthesis resulted in a mixed morphology comprised of nanoparticles and nanorods with somewhat larger feature sizes than the ammonia-based product. Because the ammonia-based catalyst gave smaller and more homogeneous particles, it was used as the primary basis for subsequent studies of carbon incorporation.

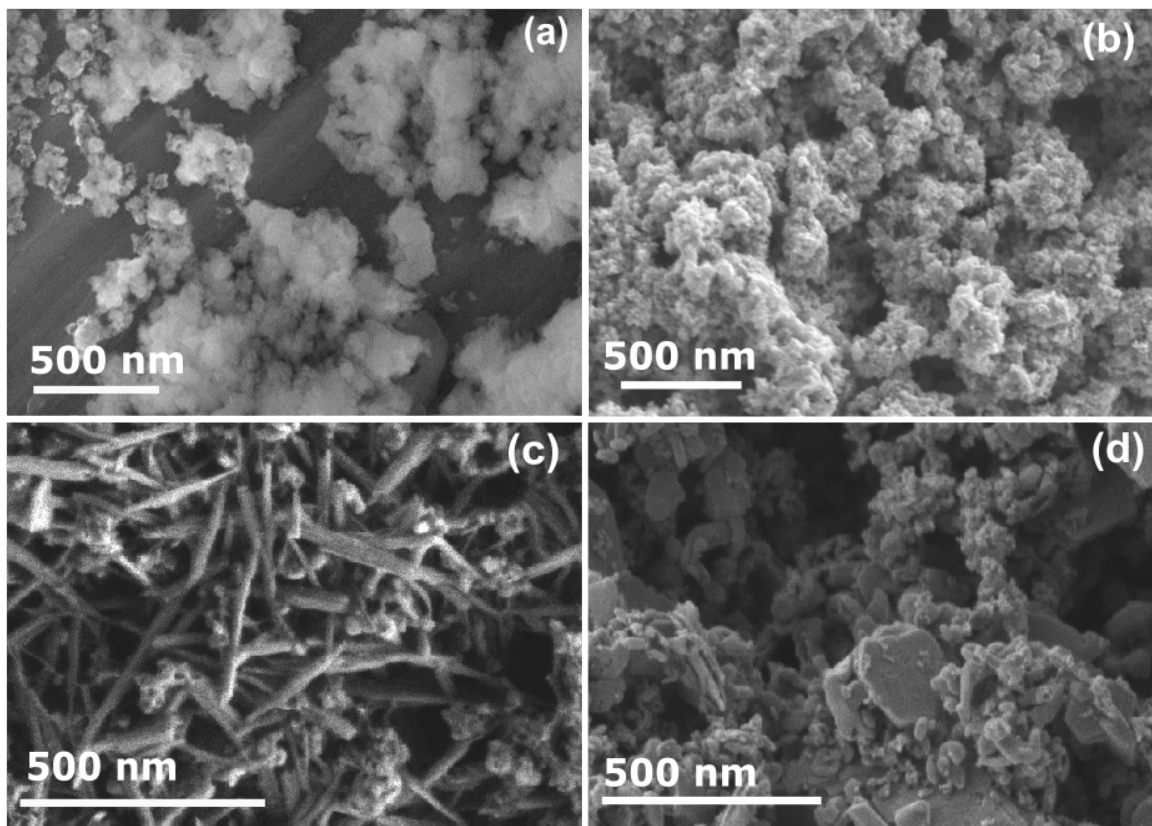


Figure 2: SEM images of oxide precipitates and reduced powders generating by two synthetic routes: (a) ammonia-based Ni-Mo oxide; (b) ammonia-based Ni-Mo; (c) ammonia-free Ni-Mo oxide; and (d) ammonia-free Ni-Mo.

We characterized the distribution of Ni-Mo and C in ammonia-based Ni-Mo/C composites using SEM imaging with a backscatter detector, as shown in Figure 3. This detector is sensitive to atomic number, where heavier elements give increased backscatter intensity, leading to lighter regions in the associated micrographs. Figure 3a,c shows backscatter images of Ni-Mo/C samples containing 75 wt% and 25 wt% carbon respectively. These images suggest that the Ni-Mo/C composites consisted of micron-scale Ni-Mo agglomerates that were homogeneously distributed with carbon over the length-scale of tens of microns. SEM images taken at higher magnification using a secondary-electron detector (Figure 3b,d) confirm that the Ni-Mo component, which exhibits characteristically smaller particle sizes than Vulcan carbon, remained as irregular agglomerates several hundred nm in diameter.

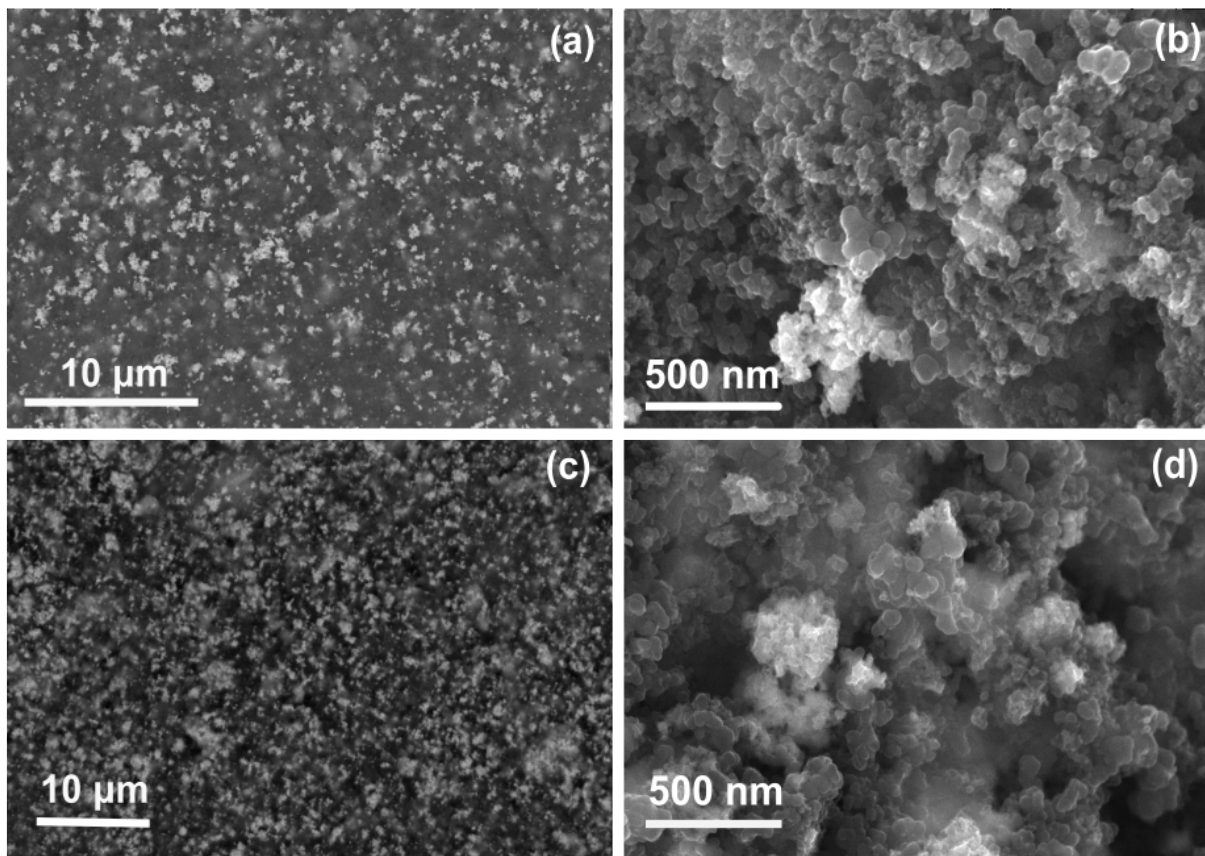


Figure 3: SEM images of ammonia-based Ni–Mo/C samples containing two different carbon loadings. Panels (a) and (b) are of a sample containing 75 wt% carbon, while panels (c) and (d) are of a sample containing 25 wt% carbon. The left images (a, c) were taken using a backscatter detector, in which Ni–Mo appears brighter than carbon, while the right images (b, d) were taken using a secondary-electron detector.

TEM analysis was used to probe the nanoscale composition and morphology of a representative sample of ammonia-based Ni–Mo nanopowder. This examination revealed that the Ni–Mo agglomerates in fact consisted of Ni-rich nanoparticles encased in a Mo-rich oxide matrix. Examples of the predominant morphology are shown in Figure 4, where one such Ni-rich nanoparticle is indicated by a white arrow, and the oxide surrounding it by a black arrow. The Ni-rich nanoparticles were convex and a few tens of nm in size. Most of these Ni-rich nanoparticles came in close contact with at least one other nanoparticle, effectively forming connected chains, though nanoparticles on the periphery of these aggregates were

more likely to be isolated by an oxide layer. Consistent with XRD results, electron diffraction showed that the Ni-rich nanoparticles were crystalline with the fcc structure and the Mo-rich oxide was nanocrystalline with ultra-fine grains. The Mo-rich oxide coating varied in thickness from near zero to a few nm, but appeared to fully enclose the Ni-rich phase in nearly all areas.

The elemental identity and distribution of the nanoparticles and oxide were verified via energy-dispersive x-ray spectroscopy (EDS) mapping, as shown in Figure 5. The maps confirm that the interior nanoparticles were strongly Ni-rich, while the co-localization of the Mo and O—but not Ni—confirm a Mo-rich oxide matrix into which the nanoparticles were embedded. Similar results were found for the ammonia-free Ni–Mo nanopowder product (see Supporting Information).

Figure 6a compares the mass-specific activity of representative ammonia-based Ni–Mo films, along with pure Ni and Pt/C controls, toward hydrogen evolution in 0.1 M aqueous KOH electrolyte. Carbon-supported Pt exhibited by far the highest HER activity, which agrees with prior reports showing Pt is considerably more active than any known non-precious HER catalyst even though it is less active in base than it is in acid.⁷⁵ Pure Ni gave the lowest mass-activity by a considerable margin. We attribute this to the relatively low intrinsic activity of Ni along with the fact that our synthesis resulted in much larger particle sizes (i.e., smaller specific surface area) than for Ni–Mo or Pt. Ni–Mo nanopowder films containing the as-synthesized catalyst also gave rather low mass activity. Hydrogen-annealed Ni–Mo films gave HER activities that were comparable to values that have been reported previously (~ 10 mA/mg at 100 mV overpotential).⁷⁰ By contrast, Ni–Mo/C films containing 75 wt% carbon were considerably more active than hydrogen annealed Ni–Mo when normalized to the mass of the Ni–Mo component.

Figure 6b compares the geometric activities of Ni–Mo catalysts synthesized by the two different routes with and without incorporation of carbon at a 3:1 mass ratio with Ni–Mo. The total catalyst mass loading was held constant at 1 mg/cm². Interestingly, the ammonia-

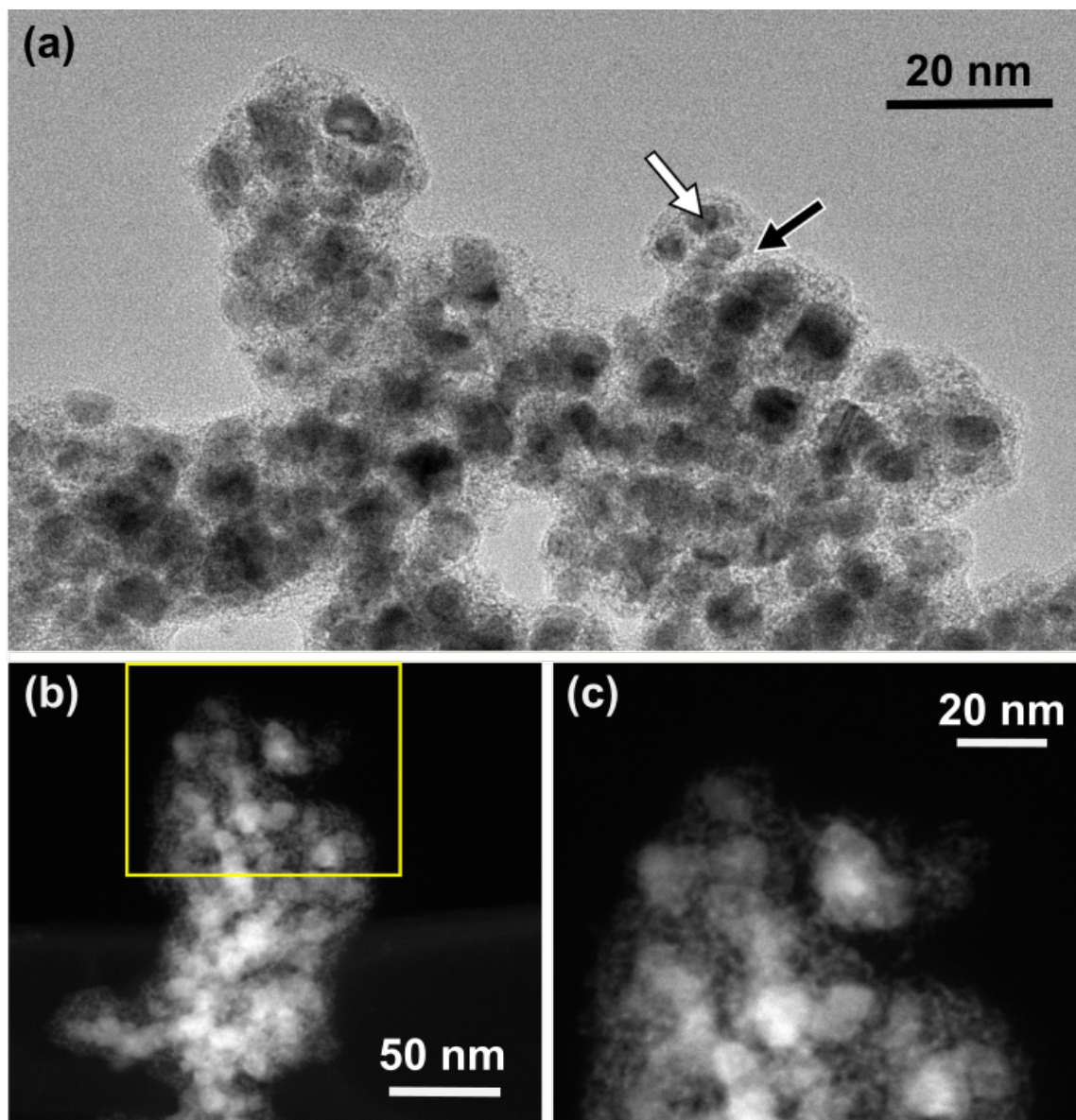


Figure 4: (a) Bright-field TEM image of ammonia-based Ni-Mo, showing Ni-rich particles (white arrow) surrounded by Mo-rich oxide (black arrow). (b) Dark-field STEM image from the same ammonia-based Ni-Mo sample, and (c) detail of the region highlighted in (b).

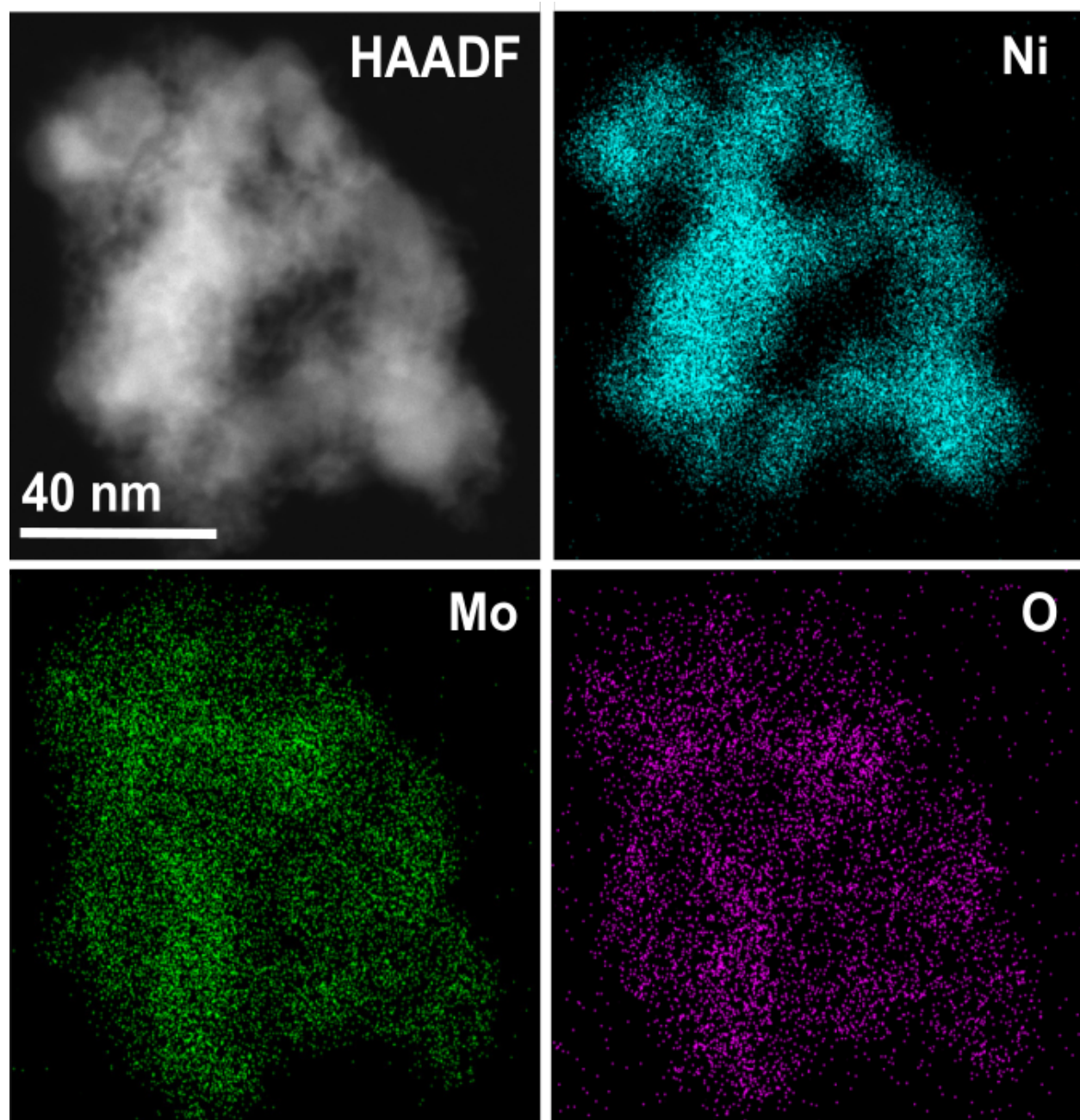


Figure 5: HAADF STEM image of single ammonia-based Ni–Mo agglomerate along with corresponding EDS elemental maps of the spatial distribution of Ni, Mo and O.

based Ni–Mo catalyst films gave essentially identical geometric activities in spite of the fact that the carbon-containing sample had only 25 % of the catalyst loading per unit electrode area. Thus, the implied specific activity was indeed considerably higher even though the chemical composition of the Ni–Mo component was indistinguishable by XRD or electron microscopy. Similar results were observed for the ammonia-free Ni–Mo samples, where carbon-containing films showed only ~ 2 -fold lower geometric activity than films without carbon despite the 4-fold reduction in Ni–Mo mass loading.

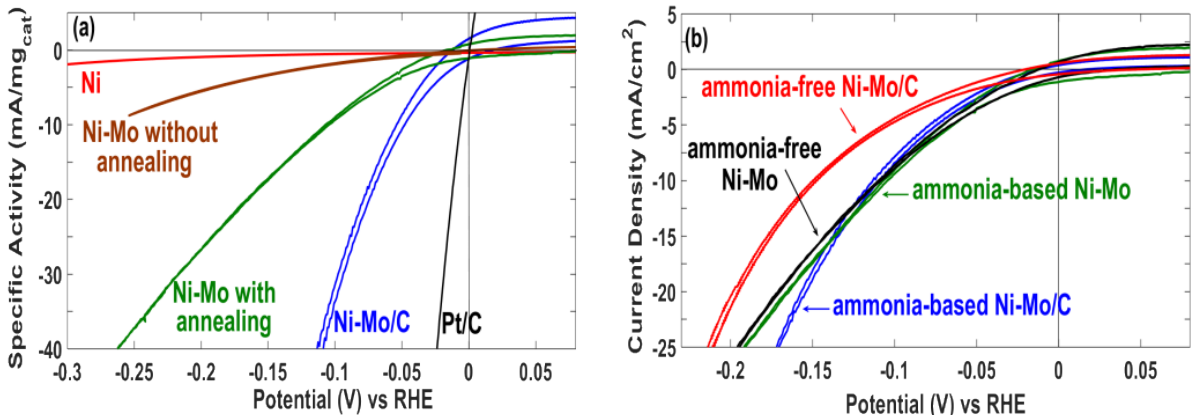


Figure 6: (a) Polarization data normalized to catalyst mass (total mass less the carbon component) for ammonia-based Ni–Mo films prepared three ways along with Ni and Pt controls. (b) Geometric activity of Ni–Mo films synthesized by both routes with and without carbon additives. All curves were collected in 0.1 M KOH solution using a scan rate of 10 mV/s and corrected for solution resistance. Total mass loadings were 1 mg/cm² in all cases except for Pt, which was 0.04 mg/cm². For Ni–Mo samples containing carbon, the carbon loading was 75 wt% relative to total catalyst mass.

To further assess the effects of carbon incorporation, we systematically varied the carbon loading in ammonia-based Ni–Mo over the range from 0 to 90 wt%. Results are shown in Figure 7 as geometric polarization data and mass activity at 100 mV overpotential. The observed geometric activity first increased with carbon incorporation up to a maximum at 50 wt% carbon, and then decreased at 75 and 90 wt% carbon loading. Furthermore, upon normalization to Ni–Mo mass, the 75 wt% carbon sample exhibited the highest apparent activity, exceeding 25 mA/mg at 100 mV overpotential.

These data collectively lead us to conclude that the observed catalytic activity in unsup-

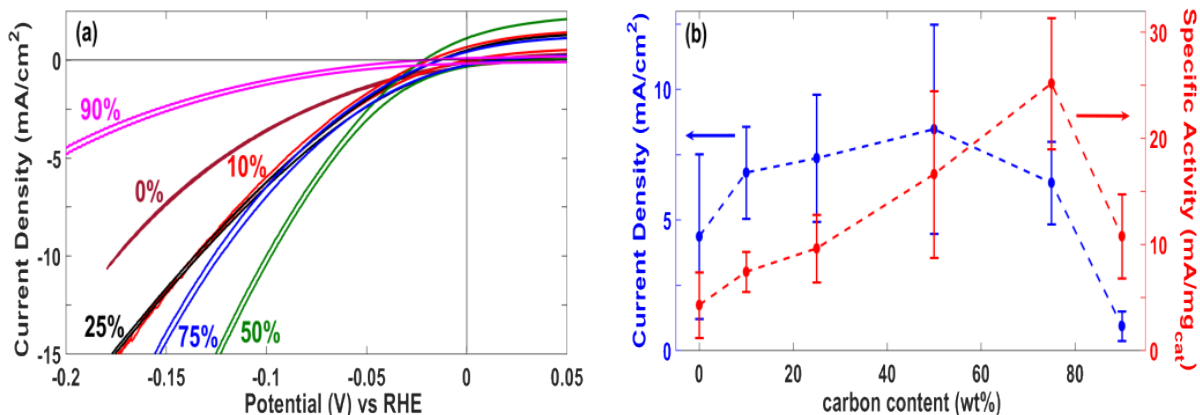


Figure 7: HER activity of ammonia-based Ni–Mo films as a function of carbon loading: (a) polarization data normalized to geometric surface area, collected under the same conditions as in Figure 6; (b) geometric current density (left axis) and Ni–Mo mass-specific current (right axis) at 100 mV overpotential as a function of carbon content. Error bars in (b) are one standard deviation from the mean of 9 samples each.

ported Ni–Mo nanopowders is limited by electrical resistivity within the catalyst film rather than reaction kinetics or transport within the electrolyte. The strongest evidence for this conclusion are the data in Fig 7a, which show that replacing active catalyst with carbon black leads to increased geometric activity. We postulate that carbon provides percolative pathways for electron conduction throughout the catalyst film, thereby mitigating solid-state resistivity limitations that result from the need to transfer electrons through the oxide layers that coat the Ni–Mo agglomerates. However, we also found that the mass-specific activity of Ni–Mo/C catalyst containing 75 wt% carbon was essentially identical to that of a carbon-free Ni–Mo in which the catalytic coating was synthesized by pyrolysis-reduction directly on a Ni mesh substrate, as shown in Figure 8. In this case we postulate that catalyst sintering during thermal reduction results in unbroken pathways for electron migration from the substrate into the catalyst coating. The same sintering effect likely occurs when nanopowders are annealed under a hydrogen atmosphere, which explains why this process activates the catalyst toward the HER, albeit not as effectively as carbon supports. We also found that carbon-free nanopowders often exhibited pyrophoric behavior upon withdrawal to air after thermal reduction, whereas Ni–Mo/C generally did not. This may be because physical dis-

persion of the metal nanoparticles on a carbon support provided sufficient additional thermal mass and conductivity to suppress runaway oxidation.

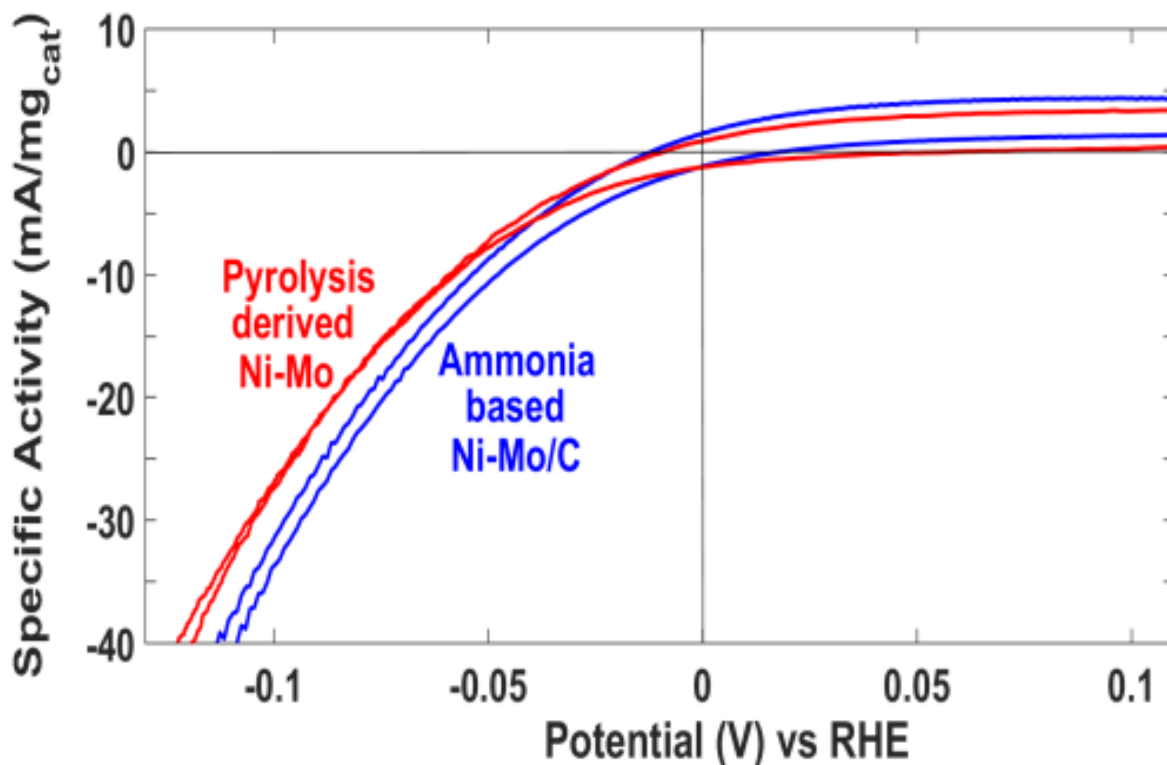


Figure 8: HER mass-specific activity of ammonia-based Ni-Mo/C compared to Ni-Mo derived from a pyrolysis-reduction method. Total mass loading was ~ 1 mg/cm² in both cases.

Another possible explanation for these observations is that the carbon support contributes significantly to the observed HER activity. However, we found that Vulcan carbon alone exhibits negligible activity toward alkaline hydrogen evolution at overpotentials below 300 mV (see Supporting Information). Additionally, if the co-deposition of Ni-Mo with carbon black activates carbon toward hydrogen evolution, we would expect normalization of observed activity to the mass of Ni-Mo alone would result a monotonic increase in HER activity as carbon loading increases. Thus, the observed decrease in activity at 90 wt% carbon is not consistent with this explanation. Instead we attribute this decrease to saturation of the conductivity enhancement accompanied by physical blocking of the Ni-Mo particles from contact with the electrolyte by excess carbon.

To further address the possibility of electrical resistivity as the predominant limiting factor in Ni–Mo nanopowder, we developed a model that describes how resistive interfaces between nanoparticles can result in diminished practical performance. This model simplifies the catalyst film to a one-dimensional string of nanoparticles attached on one side to a conductive substrate and extending into an electrolyte. The particles are comprised of a metallic core that is catalytically active and a shell that is catalytically inactive and electrically resistive while allowing facile migration of reactants to the core. Thus, upon injection of electrons from the substrate into the particle chain, they may either go on to reduce water to H₂ and OH⁻ or migrate from one particle to the next through a thin resistive interface. Neglecting transport and solution resistance losses, the HER overpotential for particle n in the string can be approximated as the sum of its kinetic and resistive components:

$$\eta_n = \eta_{n,kinetic} + \eta_{n,resistive} = b \log(i_n/i_0) + i(n \times R_{particle}) \quad (1)$$

where η is overpotential, b is Tafel slope, i_0 is exchange current density, i_n is catalytic current through particle n , and $R_{particle}$ is the interfacial resistance between each pair of particles. This equation can be solved numerically for total current by specifying particle geometry and string length along with the relevant kinetic and resistive parameters.

Using this model, we simulated HER polarization data (in terms of mass-specific current vs overpotential) using catalytic parameters corresponding to a 1 μm chain of 6 nm Ni particles surrounded by a 2 nm oxide shell with variable bulk resistivity (Figure 9a). Figure 9b shows representative results for the particles nearest and furthest from the substrate ($n = 1$ and $n = 100$, respectively) as well as the overall performance of the catalyst chain when the oxide shell had an interfacial resistivity of $10^8 \Omega\text{-cm}$. Using these parameters, the activity of the first particle was not significantly diminished by resistive losses, but the 100th particle and the overall catalyst performance were both diminished due to the need for electrons to traverse many resistive interfaces to access the entire available catalyst surface area.

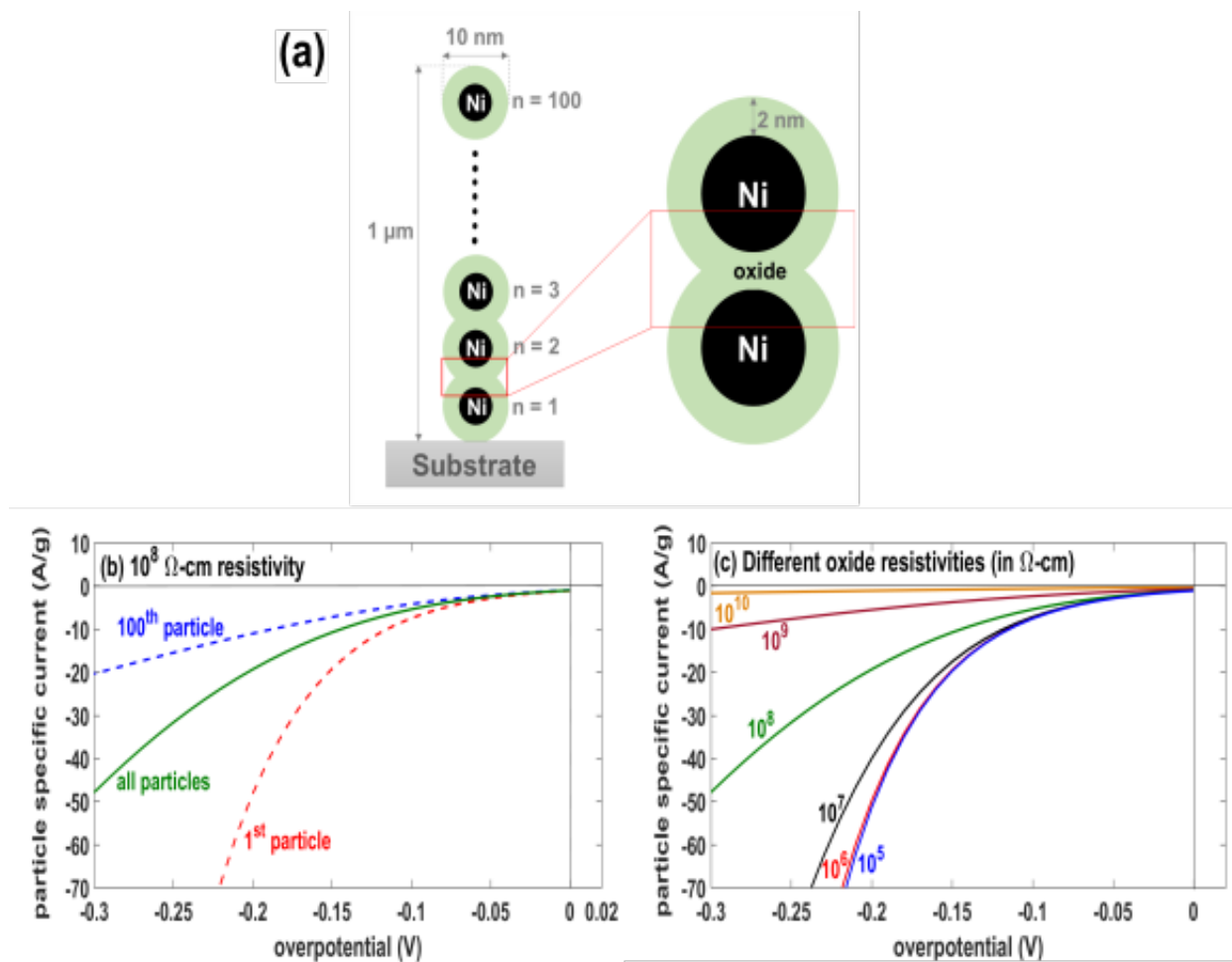


Figure 9: (a) Schematics of a 1-dimensional array of oxide-coated Ni particles stacked to make a 1 μm thick film; (b) simulated mass-specific activity of 1st, 100th and all particles using catalyst parameters approximating that of bulk Ni and an oxide resistivity of $10^8 \Omega\text{-cm}$; (c) simulated mass-specific activity of 100 particles at resistivity values over the range from 10^5 to $10^{10} \Omega\text{-cm}$.

Figure 9c compiles overall performance of the same catalyst chain using a range of resistivity values. For the specific physical dimensions we chose, oxide resistivity values exceeding $10^6 \text{ } \Omega\text{-cm}$ were necessary to observe significant resistive losses, while values above $10^9 \text{ } \Omega\text{-cm}$ were found to completely shut down catalytic activity at overpotentials below 300 mV. Importantly, these resistivity values are consistent with reported values for Ni and Mo oxides,^{76,77} which our microscopy results showed indeed encapsulate sub-10 nm alloy nanoparticles in our Ni–Mo nanopowders. These simulations also show that catalyst activity can be decreased due to interfacial resistance even without obviously exhibiting linear current-voltage behavior that is often characteristic of series resistance losses in an electrochemical experiment. Solid-state electronic conductivity limitations have been previously identified and addressed for semiconducting catalyst materials,^{21,78,79} and they are also well-known for non-precious oxide OER catalysts.^{30,32,33} However, the problem may extend even to other nominally metallic catalysts if they are synthesized as nanoparticles and coated with electrically resistive interfacial layers.

We undertook further experiments to assess the practical performance of ammonia-based Ni–Mo/C containing 75 wt% carbon as a function of catalyst layer thickness. Figure 10 compares the observed geometric HER activity at 100 mV overpotential as a function of total catalyst mass loading. Mass loadings of $\leq 1 \text{ mg/cm}^2$ used glassy carbon substrates whereas the substrate was changed to Ni mesh for higher loadings due to poor adhesion of Ni–Mo/C catalyst on glassy carbon. Increased data spread was still observed on samples with high mass loadings, which we attribute to inhomogeneous coating thicknesses and variable loss of catalyst from thick films upon handling. Nonetheless, these data are reasonably well described by a power law relationship, $J = 11m^{0.73}$, where J is geometric current density and m is total mass loading. If the catalyst were limited only by reaction kinetics at all mass loadings, this relationship would be purely linear. Deviations from linearity are expected due to emergent transport limitations, which result in “diminishing returns” in mass activity as the catalyst layer thickness and current density increase. However, in this case the deviations

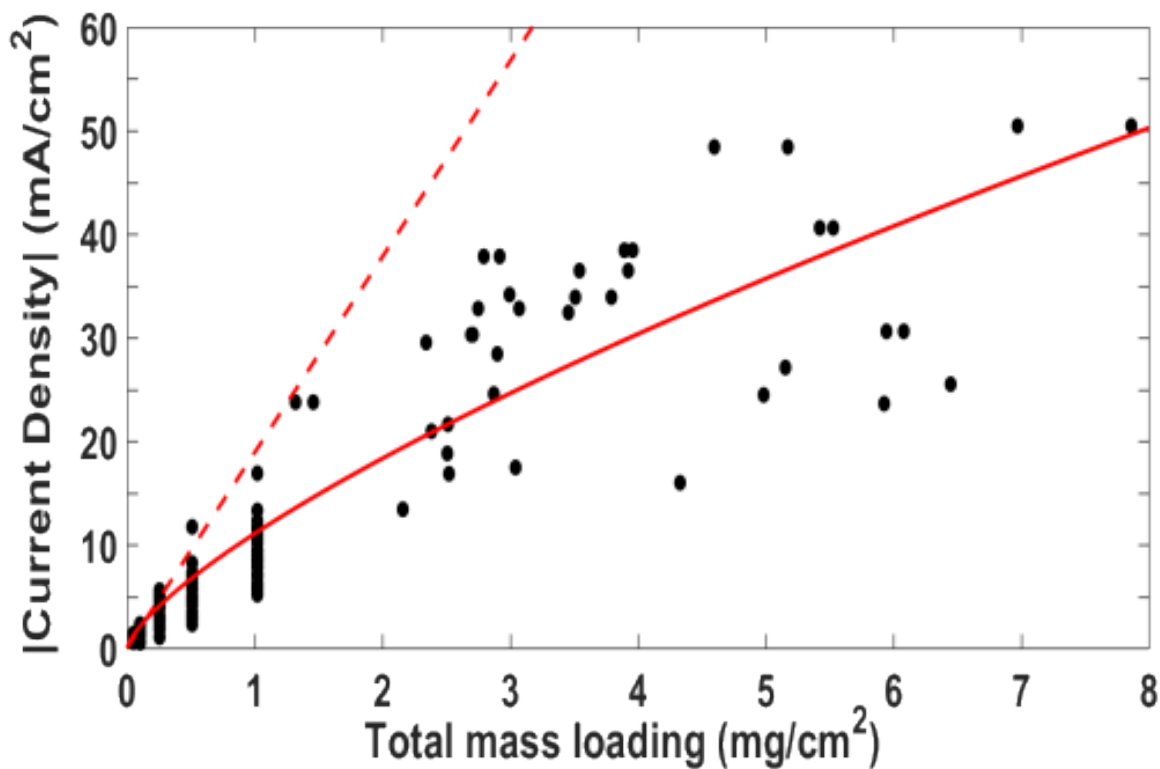


Figure 10: Geometric HER activity of ammonia-based Ni-Mo/C containing 75 wt% carbon at 100 mV overpotential as a function of total mass loading of the composite. The solid red line corresponds to the best-fit equation: $J = 11.07m^{0.7274}$, and the dotted line is a linear extrapolation between the origin and the mean of the activity data collected at 0.05 mg/cm². Glassy carbon substrates were used for loadings ≤ 1 mg/cm² and Ni mesh substrates were used for higher loadings.

from linearity become significant even at catalyst loadings well below 1 mg/cm^2 and current densities below 10 mA/cm^2 . These values are lower than the expected onset of significant transport limitations, providing evidence that even these Ni–Mo/C films still exhibit some residual resistivity in spite of the incorporation of carbon black.

The dotted line in Figure 10 corresponds to a linear fit between the origin and the mean of the observed Ni–Mo/C current density at the lowest mass loading we tested, which was $50 \text{ }\mu\text{g/cm}^2$. The slope of this line is 19 mA/mg (i.e., 76 mA/mg on the basis of Ni–Mo alone), which we took as an estimate of the achievable mass-activity of the catalyst composite even at higher mass loadings if resistive limitations could be entirely eliminated. Motivated by this result, we worked to increase the dispersion of Ni–Mo on the carbon support in an effort to improve inter-particle conductivity. Results are shown in Figure 11, which depicts polarization data and mass-activity for Ni–Mo/C films at a 1 mg/cm^2 total mass loading in which Vulcan carbon was included in the precipitation mixture rather than composited with Ni–Mo oxide by physical grinding. Remarkably, as the carbon loading increased from 9 to 80 wt%, the geometric activity decreased only by a factor of ~ 2 . Thus, mass activities normalized to Ni–Mo content were as high as 60 mA/mg_{cat} , which is ~ 6 times higher than prior results involving post-deposition annealing and over those that observed for Ni–Mo/C prepared by physical grinding. We expect that these observed values still represent a lower bound estimate of the true HER mass activity of Ni–Mo nanopowders prepared in this way.

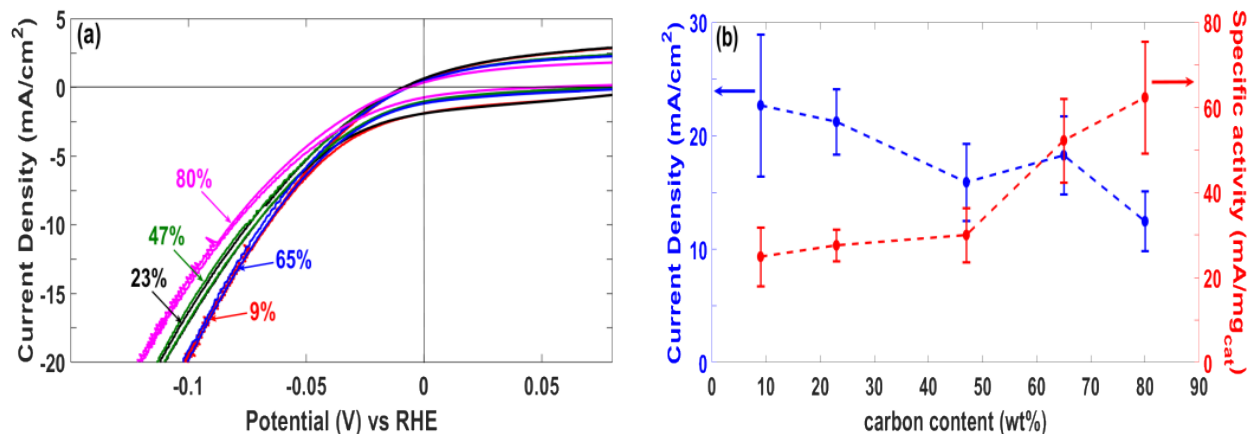


Figure 11: HER activity of ammonia-based Ni–Mo films prepared by co-precipitation with Vulcan carbon as a function of carbon loading: (a) polarization data normalized to geometric surface area, collected under the same conditions as in Figure 6; (b) geometric current density (left axis) and mass-specific current (right axis) at 100 mV overpotential as a function of catalyst mass. Error bars in (b) are one standard deviation from the mean of 3–7 samples.

Conclusions

We synthesized and characterized Ni–Mo alloy nanopowder electrocatalysts by sequential precipitation-reduction from homogeneous precursors with and without the addition of ammonia as a solubilizing agent. The composition and morphology of ammonia-based and ammonia-free Ni–Mo catalysts were similar, consisting of Ni-rich alloy nanoparticles embedded in a matrix of Mo-rich oxides. Using a combination of experiments and straightforward modeling, we compiled evidence that inter-particle resistivity limits their observed activity toward alkaline hydrogen evolution. The effects of these resistive interfaces can be ameliorated by synthesizing the catalyst directly on a metallic current collector, by thermally annealing the catalyst after deposition, or by adding carbon black as a conductive support. Well-dispersed catalysts on carbon black were found to exhibit greatly increased HER activity when normalized to catalyst mass, but geometric activities remain modest due to the need to incorporate a significant fraction of carbon in the active catalyst film. Nevertheless, carbon compositing eliminates the need for thermal processing after catalyst deposition,

which makes Ni–Mo/C catalysts compatible with diverse substrates, including polymeric membranes as are used in AAEM electrolyzers. Additional work is warranted to further mitigate interfacial resistive effects in Ni–Mo and to address the possibility that resistive losses limit the performance of other nominally metallic HER catalysts. Additional work is also needed to improve catalyst processing and coating methods to increase geometric current densities while keeping catalyst layers thin enough to avoid transport limitations.

Acknowledgement

RBP, AM and JRM acknowledge support from McKone Laboratory start-up funds provided by University of Pittsburgh, Swanson School of Engineering. JCY and SDH acknowledge the support of NSF DMREF through contract No. CHE-1534630 and the ETEM Catalysis Consortium (ECC), funded through the University of Pittsburgh and Hitachi High Technologies Corp. The TEM work was performed at the Nanoscale Fabrication and Characterization Facility, a laboratory of the Gertrude E. and John M. Petersen Institute of NanoScience and Engineering, housed at the University of Pittsburgh. We also acknowledge Prof. Götz Vesper for assistance with TGA measurements and Prof. Alexander Star for assistance with Ultramicrobalance.

References

- (1) Satyapal, S. Hydrogen and Fuel Cells Overview. Presented at DLA Worldwide Energy Conference, National Harbor, MD, April 10-12, 2017.
- (2) Valladares, M.-R. d. Global Trends and Outlook for Hydrogen. IEA Hydrogen, December 2017. p 6.
- (3) Pivovar, B.; Rustagi, N.; Satyapal, S. Hydrogen at Scale (H2 @Scale) Key to a Clean,

- Economic, and Sustainable Energy System. *Electrochemical Society Interface* **2018**, *27*, 47–52.
- (4) Grundt, T.; K., C. Hydrogen by water electrolysis as basis for small scale Ammonia production. A comparison with Hydrocarbon based technologies. *International Journal of Hydrogen Energy* **1982**, *7*, 247–257.
- (5) Bagotsky, V. S. *Fuel Cells: Problems and Solutions*, 2nd ed.; John Wiley and Sons, Inc., Hoboken, New Jersey, 2012; pp 47–51.
- (6) Ayers, K. E.; Anderson, E. B.; Capuano, C.; Carter, B.; Dalton, L.; Hanlon, G.; Manco, J.; Niedzwiecki, M. Research Advances towards Low Cost, High Efficiency PEM Electrolysis. *ECS Transactions* **2010**, *33*, 3–15.
- (7) Ito, H.; Miyazaki, N.; Sugiyama, S.; Ishida, M.; Nakamura, Y.; Iwasaki, S.; Hasegawa, Y.; Nakano, A. Investigations on electrode configurations for anion exchange membrane electrolysis. *Journal of Applied Electrochemistry* **2018**, *48*, 305–316.
- (8) Phillips, R.; Dunnill, C. W. Zero gap alkaline electrolysis cell design for renewable energy storage as hydrogen gas. *RSC Advances* **2016**, *6*, 100643–100651.
- (9) Marini, S.; Salvi, P.; Nelli, P.; Pesenti, R.; Villa, M.; Berrettoni, M.; Zangari, G.; Kiros, Y. Advanced alkaline water electrolysis. *Electrochimica Acta* **2012**, *82*, 384–391.
- (10) Xiao, L.; Zhang, S.; Pan, J.; Yang, C.; He, M.; Zhuang, L.; Lu, J. First implementation of alkaline polymer electrolyte water electrolysis working only with pure water. *Energy & Environmental Science* **2012**, *5*, 7869.
- (11) Lu, S. F.; Pan, J.; Huang, a. B.; Zhuang, L.; Lu, J. T. Alkaline polymer electrolyte fuel cells completely free from noble metal catalysts. *Proceedings of the National Academy of Sciences of the United States of America* **2008**, *105*, 20611–20614.

- (12) Wang, Y.-J.; Qiao, J.; Baker, R.; Zhang, J. Alkaline polymer electrolyte membranes for fuel cell applications. *Chemical Society Reviews* **2013**, *42*, 5768.
- (13) Pletcher, D.; Li, X. Prospects for alkaline zero gap water electrolyzers for hydrogen production. *International Journal of Hydrogen Energy* **2011**, *36*, 15089–15104.
- (14) Merle, G.; Wessling, M.; Nijmeijer, K. Anion exchange membranes for alkaline fuel cells: A review. *Journal of Membrane Science* **2011**, *377*, 1–35.
- (15) Robertson, N. J.; Kostalik, H. A.; Clark, T. J.; Mutolo, P. F.; Abruña, H. D.; Coates, G. W.; Abruña, H. D.; Coates, G. W. Tunable high performance cross-linked alkaline anion exchange membranes for fuel cell applications. *Journal of the American Chemical Society* **2010**, *132*, 3400–3404.
- (16) Pan, J.; Lu, S.; Li, Y.; Huang, A.; Zhuang, L.; Lu, J. High-Performance alkaline polymer electrolyte for fuel cell applications. *Advanced Functional Materials* **2010**, *20*, 312–319.
- (17) Mahmood, N.; Yao, Y.; Zhang, J. W.; Pan, L.; Zhang, X.; Zou, J. J. Electrocatalysts for Hydrogen Evolution in Alkaline Electrolytes: Mechanisms, Challenges, and Prospective Solutions. *Advanced Science* **2018**, *5*.
- (18) He, B.; Kuang, Y.; Hou, Z.; Zhou, M.; Chen, X. Enhanced electrocatalytic hydrogen evolution activity of nickel foam by low-temperature-oxidation. *Journal of Material Research* **2017**, *33*, 213–224.
- (19) Safizadeh, F.; Ghali, E.; Houlachi, G. Electrocatalysis developments for hydrogen evolution reaction in alkaline solutions - A Review. *International Journal of Hydrogen Energy* **2015**, *40*, 256–274.
- (20) McCrory, C. C. L.; Jung, S.; Ferrer, I. M.; Chatman, S. M.; Peters, J. C.; Jaramillo, T. F. Benchmarking Hydrogen Evolving Reaction and Oxygen Evolving

- Reaction Electrocatalysts for Solar Water Splitting Devices. *Journal of the American Chemical Society* **2015**, *137*, 4347–4357.
- (21) Laursen, A. B.; Patraju, K. R.; Whitaker, M. J.; Retuerto, M.; Sarkar, T.; Yao, N.; Ramanujachary, K. V.; Greenblatt, M.; Dismukes, G. C. Nanocrystalline Ni₅P₄: A hydrogen evolution electrocatalyst of exceptional efficiency in both alkaline and acidic media. *Energy and Environmental Science* **2015**, *8*, 1027–1034.
- (22) Gong, M.; Zhou, W.; Tsai, M. C.; Zhou, J.; Guan, M.; Lin, M. C.; Zhang, B.; Hu, Y.; Wang, D. Y.; Yang, J.; Pennycook, S. J.; Hwang, B. J.; Dai, H. Nanoscale nickel oxide/nickel heterostructures for active hydrogen evolution electrocatalysis. *Nature Communications* **2014**, *5*, 1–6.
- (23) Lv, X. J.; She, G. W.; Zhou, S. X.; Li, Y. M. Highly efficient electrocatalytic hydrogen production by nickel promoted molybdenum sulfide microspheres catalysts. *RSC Advances* **2013**, *3*, 21231–21236.
- (24) Vrabel, H.; Hu, X. Molybdenum boride and carbide catalyze hydrogen evolution in both acidic and basic solutions. *Angewandte Chemie - International Edition* **2012**, *51*, 12703–12706.
- (25) Danilovic, N.; Subbaraman, R.; Strmcnik, D.; Chang, K. C.; Paulikas, A. P.; Stamenkovic, V. R.; Markovic, N. M. Enhancing the alkaline hydrogen evolution reaction activity through the bifunctionality of Ni(OH)₂/metal catalysts. *Angewandte Chemie - International Edition* **2012**, *51*, 12495–12498.
- (26) Li, Y.; Wang, H.; Xie, L.; Liang, Y.; Hong, G.; Dai, H. MoS₂ nanoparticles grown on graphene: An advanced catalyst for the hydrogen evolution reaction. *Journal of the American Chemical Society* **2011**, *133*, 7296–7299.
- (27) Klaus, S.; Cai, Y.; Louie, M. W.; Trotochaud, L.; Bell, A. T. Effects of Fe electrolyte

- impurities on Ni(OH)₂/NiOOH structure and oxygen evolution activity. *Journal of Physical Chemistry C* **2015**, *119*, 7243–7254.
- (28) Gong, M.; Dai, H. A mini review of NiFe-based materials as highly active oxygen evolution reaction electrocatalysts. *Nano Research* **2015**, *8*, 23–39.
- (29) Friebel, D.; Louie, M. W.; Bajdich, M.; Sanwald, K. E.; Cai, Y.; Wise, A. M.; Cheng, M. J.; Sokaras, D.; Weng, T. C.; Alonso-Mori, R.; Davis, R. C.; Bargar, J. R.; Nørskov, J. K.; Nilsson, A.; Bell, A. T. Identification of highly active Fe sites in (Ni,Fe)OOH for electrocatalytic water splitting. *Journal of the American Chemical Society* **2015**, *137*, 1305–1313.
- (30) Burke, M. S.; Enman, L. J.; Batchellor, A. S.; Zou, S.; Boettcher, S. W. Oxygen Evolution Reaction Electrocatalysis on Transition Metal Oxides and (Oxy)hydroxides: Activity Trends and Design Principles. *Chemistry of Materials* **2015**, *27*, 7549–7558.
- (31) Burke, M. S.; Zou, S.; Enman, L. J.; Kellon, J. E.; Gabor, C. A.; Pledger, E.; Boettcher, S. W. Revised Oxygen Evolution Reaction Activity Trends for First-Row Transition-Metal (Oxy)hydroxides in Alkaline Media. *Journal of Physical Chemistry Letters* **2015**, *6*, 3737–3742.
- (32) Trotochaud, L.; Boettcher, S. W. Precise oxygen evolution catalysts: Status and opportunities. *Scripta Materialia* **2014**, *74*, 25–32.
- (33) Trotochaud, L.; Young, S. L.; Ranney, J. K.; Boettcher, S. W. Nickel-Iron oxyhydroxide oxygen-evolution electrocatalysts: The role of intentional and incidental iron incorporation. *Journal of the American Chemical Society* **2014**, *136*, 6744–6753.
- (34) McCrory, C. C. L.; Jung, S.; Peters, J. C.; Jaramillo, T. F. Benchmarking Heterogeneous Electrocatalysts for the Oxygen Evolution Reaction. *Journal of the American Chemical Society* **2013**, *135*, 16977–16987.

- (35) Louie, M. W.; Bell, A. T. An investigation of thin-film Ni-Fe oxide catalysts for the electrochemical evolution of oxygen. *Journal of the American Chemical Society* **2013**, *135*, 12329–12337.
- (36) Gong, M.; Li, Y.; Wang, H.; Liang, Y.; Wu, J. Z.; Zhou, J.; Wang, J.; Regier, T.; Wei, F.; Dai, H. An advanced Ni-Fe layered double hydroxide electrocatalyst for water oxidation. *Journal of the American Chemical Society* **2013**, *135*, 8452–8455.
- (37) Corrigan, D. A. The Catalysis of the Oxygen Evolution Reaction by Iron Impurities in Thin Film Nickel Oxide Electrodes. *Journal of The Electrochemical Society* **1987**, *134*, 377.
- (38) Zeng, M.; Li, Y. Recent advances in heterogeneous electrocatalysts for the hydrogen evolution reaction. *Journal of Materials Chemistry A* **2015**, *3*, 14942–14962.
- (39) Brown, D. E.; Mahmood, M. N.; Man, M. C. M.; Turner, A. K. Preparation and characterization of low overvoltage transition metal alloy electrocatalysts for hydrogen evolution in alkaline solutions. *Electrochimica Acta* **1984**, *29*, 1551–1556.
- (40) Raj, I. A. Nickel-based, binary-composite electrocatalysts for the cathodes in the energy-efficient industrial production of hydrogen from alkaline-water electrolytic cells. *Journal of Materials Science* **1993**, *28*, 4375–4382.
- (41) Raj, I. A.; Vasu, K. I. Transition metal-based hydrogen electrodes in alkaline solution - electrocatalysis on nickel based binary alloy coatings. *Journal of Applied Electrochemistry* **1990**,
- (42) Arul Raj, I.; Venkatesan, V. K. Characterization of nickel-molybdenum and nickel-molybdenum-iron alloy coatings as cathodes for alkaline water electrolyzers. *International Journal of Hydrogen Energy* **1988**, *13*, 215–223.

- (43) Gao, M. Y.; Yang, C.; Zhang, Q. B.; Zeng, J. R.; Li, X. T.; Hua, Y. X.; Xu, C. Y.; Dong, P. Facile electrochemical preparation of self-supported porous Ni-Mo alloy microspheres as efficient bifunctional electrocatalysts for water splitting. *Journal of Materials Chemistry A* **2017**, *5*, 5797–5805.
- (44) Wang, Y.; Zhang, G.; Xu, W.; Wan, P.; Lu, Z.; Li, Y.; Sun, X. A 3D Nanoporous Ni-Mo Electrocatalyst with Negligible Overpotential for Alkaline Hydrogen Evolution. *ChemElectroChem* **2014**, *1*, 1138–1144.
- (45) Zhang, J.; Wang, T.; Liu, P.; Liao, Z.; Liu, S.; Zhuang, X.; Chen, M.; Zschech, E.; Feng, X. Efficient hydrogen production on MoNi₄ electrocatalysts with fast water dissociation kinetics. *Nature Communications* **2017**, *8*, 15437.
- (46) Zhou, H.; Yu, F.; Zhu, Q.; Sun, J.; Qin, F.; Yu, L.; Bao, J.; Yu, Y.; Chen, S.; Ren, Z. Water splitting by electrolysis at high current densities under 1.6 volts. *Energy & Environmental Science* **2018**, 3–5.
- (47) Zhao, S.; Huang, J.; Liu, Y.; Shen, J.; Wang, H.; Yang, X.; Zhu, Y.; Li, C. Multimetallic NiMo/Cu nanowires as nonprecious and efficient full water splitting catalyst. *J. Mater. Chem. A* **2017**, *5*, 4207–4214.
- (48) Shetty, S.; Mohamed Jaffer Sadiq, M.; Bhat, D. K.; Hegde, A. C. Electrodeposition and characterization of Ni-Mo alloy as an electrocatalyst for alkaline water electrolysis. *Journal of Electroanalytical Chemistry* **2017**, *796*, 57–65.
- (49) Schalenbach, M.; Speck, F. D.; Ledendecker, M.; Kasian, O.; Goehl, D.; Mingers, A. M.; Breitbach, B.; Springer, H.; Cherevko, S.; Mayrhofer, K. J. Nickel-molybdenum alloy catalysts for the hydrogen evolution reaction: Activity and stability revised. *Electrochimica Acta* **2017**, *259*, 1154–1161.
- (50) Jin, Y.; Yue, X.; Shu, C.; Huang, S.; Shen, P. K. Three-dimensional porous MoNi₄

- networks constructed by nanosheets as bifunctional electrocatalysts for overall water splitting. *J. Mater. Chem. A* **2017**, *5*, 2508–2513.
- (51) Csernica, P. M.; McKone, J. R.; Mulzer, C. R.; Dichtel, W. R.; Abruña, H. D.; DiSalvo, F. J. Electrochemical Hydrogen Evolution at Ordered Mo₇Ni₇. *ACS Catalysis* **2017**, *7*, 3375–3383.
- (52) Xu, C.; Zhou, J. b.; Zeng, M.; Fu, X. l.; Liu, X. j.; Li, J. m. Electrodeposition mechanism and characterization of NiMo alloy and its electrocatalytic performance for hydrogen evolution. *International Journal of Hydrogen Energy* **2016**, *41*, 13341–13349.
- (53) Zhang, L.; Xiong, K.; Nie, Y.; Wang, X.; Liao, J.; Wei, Z. Sputtering nickel-molybdenum nanorods as an excellent hydrogen evolution reaction catalyst. *Journal of Power Sources* **2015**, *297*, 413–418.
- (54) Tian, J.; Cheng, N.; Liu, Q.; Sun, X.; He, Y.; Asiri, A. M. Self-supported NiMo hollow nanorod array: an efficient 3D bifunctional catalytic electrode for overall water splitting. *J. Mater. Chem. A* **2015**, *3*, 20056–20059.
- (55) McKone, J. R.; Marinescu, S. C.; Brunschwig, B. S.; Winkler, J. R.; Gray, H. B. Earth-abundant hydrogen evolution electrocatalysts. *Chemical Science* **2014**, *5*, 865–878.
- (56) Cristina González-Buch, E. M. O., Isaac Herraiz-Cardona; José García-Antón, V. P.-H. Development of Ni-Mo, Ni-W and Ni-Co macroporous materials for hydrogen evolution reaction. *Chemical Engineering Transactions* **2013**, *32*, 865–870.
- (57) Han, Q.; Cui, S.; Pu, N.; Chen, J.; Liu, K.; Wei, X. A study on pulse plating amorphous NiMo alloy coating used as HER cathode in alkaline medium. *International Journal of Hydrogen Energy* **2010**, *35*, 5194–5201.
- (58) Krstajić, N. V.; Jović, V. D.; Gajić-Krstajić, L.; Jović, B. M.; Antozzi, A. L.; Martelli, G. N. Electrodeposition of Ni-Mo alloy coatings and their characterization

- as cathodes for hydrogen evolution in sodium hydroxide solution. *International Journal of Hydrogen Energy* **2008**, *33*, 3676–3687.
- (59) N.Krstajić,; M.Popović,; B.Grgur,; M.Vojnović,; D.Šepa, On the kinetics of the hydrogen evolution reaction on nikel in alkaline solution. Part I. The mechanism. *Journal of Electroanalytical Chemistry* **2001**, *512*, 16–26.
- (60) Gennero de Chialvo, M.; Chialvo, A. Hydrogen evolution reaction on smooth Ni(1x)+Mo(x) alloys (0x0.25). *Journal of Electroanalytical Chemistry* **1998**, *448*, 87–93.
- (61) Kawashima, A.; Akiyama, E.; Habazaki, H.; Hashimoto, K. Characterization of sputter-deposited Ni-Mo and Ni-W alloy electrocatalysts for hydrogen evolution in alkaline solution. *Materials Science and Engineering: A* **1997**, *226-228*, 905–909.
- (62) Hu, W.; Cao, X.; Wang, F.; Zhang, Y. A novel cathode for alkaline water electrolysis. *International Journal of Hydrogen Energy* **1997**, *22*, 621–623.
- (63) Fan, C. Study of Electrodeposited Nickel-Molybdenum, Nickel-Tungsten, Cobalt-Molybdenum, and Cobalt-Tungsten as Hydrogen Electrodes in Alkaline Water Electrolysis. *Journal of The Electrochemical Society* **1994**, *141*, 382.
- (64) Huot, J.; Trudeau, M.; Schulz, R. Low Hydrogen Overpotential Nanocrystalline Ni-Mo Cathodes for Alkaline Water Electrolysis. *Journal of The Electrochemical Society* **1991**, *138*, 1316–1321.
- (65) Divisek, J.; Schmitz, H.; Balej, J. Ni and Mo coatings as hydrogen cathodes. *Journal of Applied Electrochemistry* **1989**, *19*, 519–530.
- (66) Tilak, B. V.; Conway, B. E. High performance electrode materials for the hydrogen evolution reaction from alkaline media. *Proc. Indian Acad. Sci. (Chem. Sci.)* **1986**, *97*, 359–393.

- (67) Stachurski, D.; Pouli, G.; Pokrzyk, G.; Ripas, J. Low overvoltage hydrogen cathodes. U.S. Patent 4,354,915, October 19, 1982.
- (68) Brown, D. E.; Mahmood, M. N. Method of Preparing Active Electrodes. U.S. Patent 4,358,475, November 9, 1982.
- (69) Brown, D.; Mahmood, M.; Turner, A.; Hall, S.; Fogarty, P. Low overvoltage electrocatalysts for hydrogen evolving electrodes. *International Journal of Hydrogen Energy* **1982**, *7*, 405–410.
- (70) McKone, J. R.; Sadtler, B. F.; Werlang, C. A.; Lewis, N. S.; Gray, H. B. Ni-Mo nanopowders for efficient electrochemical hydrogen evolution. *ACS Catalysis* **2013**, *3*, 166–169.
- (71) Shaner, M. R.; McKone, J. R.; Gray, H. B.; Lewis, N. S. Functional integration of NiMo electrocatalysts with Si microwire array photocathodes to simultaneously achieve high fill factors and light-limited photocurrent densities for solar-driven hydrogen evolution. *Energy & Environmental Science* **2015**, *8*, 2977–2984.
- (72) Verlage, E.; Hu, S.; Liu, R.; Jones, R. J.; Sun, K.; Xiang, C.; Lewis, N. S.; Atwater, H. A. A monolithically integrated, intrinsically safe, 10% efficient, solar-driven water-splitting system based on active, stable earth-abundant electrocatalysts in conjunction with tandem III-V light absorbers protected by amorphous TiO₂films. *Energy and Environmental Science* **2015**, *8*, 3166–3172.
- (73) Tang, X.; Xiao, L.; Yang, C.; Lu, J.; Zhuang, L. Noble fabrication of Ni-Mo cathode for alkaline water electrolysis and alkaline polymer electrolyte water electrolysis. *International Journal of Hydrogen Energy* **2014**, *39*, 3055–3060.
- (74) Brito, J. L.; Laine, J.; Pratt, K. C. Temperature-programmed reduction of Ni-Mo oxides. *Journal of Materials Science* **1989**, *24*, 425–431.

- (75) Sheng, W.; Gasteiger, H. A.; Shao-Horn, Y. Hydrogen Oxidation and Evolution Reaction Kinetics on Platinum: Acid vs Alkaline Electrolytes. *Journal of The Electrochemical Society* **2010**, *157*, B1529.
- (76) Morin, F. J. Electrical properties of NiO. *Physical Review* **1954**, *93*, 1199–1204.
- (77) Deb, S. K.; Chopoorian, J. A. Optical properties and color-center formation in thin films of molybdenum trioxide. *Journal of Applied Physics* **1966**, *37*, 4818–4825.
- (78) Lukowski, M. A.; Daniel, A. S.; Meng, F.; Forticaux, A.; Li, L.; Jin, S. Enhanced hydrogen evolution catalysis from chemically exfoliated metallic MoS₂ nanosheets. *Journal of the American Chemical Society* **2013**, *135*, 10274–10277.
- (79) Chen, Z.; Cummins, D.; Reinecke, B. N.; Clark, E.; Sunkara, M. K.; Jaramillo, T. F. Core-shell MoO₃-MoS₂ Nanowires for Hydrogen Evolution: A Functional Design for Electrocatalytic Materials. *Nano Letters* **2011**, *11*, 4168–4175.